CRYSTAL GROWTH & DESIGN

Article

Cite This: Cryst. Growth Des. XXXX, XXX, XXX-XXX

pubs.acs.org/crystal

Nanoscale Structure–Property Relationships in Low-Temperature Solution-Processed Electron Transport Layers for Organic Photovoltaics

Jiaqi Zhang,[†] Maurizio Morbidoni,[†] Claire H. Burgess,[†] Jiaying Wu,[‡] Tian Du,[†] Khallil Harrabi,[§] David J. Payne,[†] James R. Durrant,[‡] and Martyn A. McLachlan*[,†]

[†]Department of Materials and Centre for Plastic Electronics and [‡]Department of Chemistry and Centre for Plastic Electronics, Imperial College London, London SW7 2AZ, United Kingdom

[§]Physics Department and Center of Research Excellence in Renewable Energy, King Fahd University of Petroleum and Minerals, 31261 Dhahran, Saudi Arabia

Supporting Information

ABSTRACT: Here we elucidate the nanostructure–property relationships in low-temperature, solution-processed ZnO based thin films employed as novel electron transport layers (ETLs) in organic photovoltaic (OPV) devices. Using a low-cost zinc precursor (zinc acetate) in a simple amine–alcohol solvent mix, high-quality ETL thin films are prepared. We show that at a processing temperature of 110 °C the films are composed of nanoparticles embedded in a continuous organic matrix consisting of ZnO precursor species and stabilizers. Using a combination of transmission electron microscopy (TEM) and X-ray photoelectron spectroscopy (XPS), we study the thermally induced morphological and compositional changes in the ETLs. Transient optoelectronic probes reveal that the mixed nanocrystalline/amorphous nature of the films does not contribute to recombination losses in devices. We propose that charge transport in our low-temperature processed ETLs is facilitated by the network of ZnO nanoparticles, with the organic matrix serving to tune the work function of the ETL and to provide excellent resistance to current leakage. To demonstrate the performance of our ETLs we prepare inverted architecture OPVs utilizing Poly[[4,8-bis[(2-ethylhexyl)oxy]benzo[1,2-*b*:4,5-*b*′]dithiophene-2,6-diyl][3-fluoro-2-[(2-ethylhexyl)carbonyl]thieno[3,4-*b*]thiophenediyl]] (**PTB7**): [6,6]-Phenyl-C71-butyric acid methyl ester (**$PC_{71}BM$**) as active layer materials. The low-temperature ETL devices showed typical power conversion efficiencies (PCEs) of >7% with the champion devices achieving a PCE > 8%.

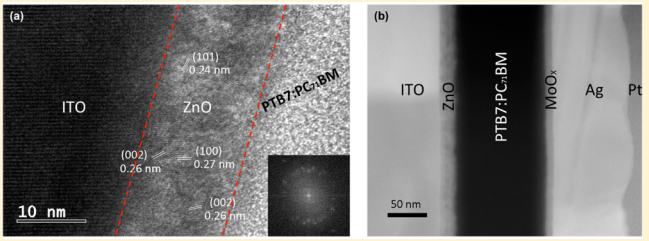

1. INTRODUCTION

Organic photovoltaic (OPV) devices are one of the key technologies to exploit the development of organic semiconducting materials. OPVs offer the potential to deliver clean, low-cost renewable energy and provide device functionality that incumbent technologies cannot, namely, their inherently lightweight nature and compatibility with solution processing on rigid *and* flexible substrates.[1−3] A significant volume of research in the synthesis of organic semiconducting polymers has been carried out over the past decade, resulting in considerable performance enhancements in OPVs, organic light emitting diodes (LEDs) and organic thin film transistors (TFTs).[4−6] More recently it has become apparent that device performance enhancements can be achieved across these technology platforms by interfacing the organic species with inorganic, particularly metal oxide, semiconductors.[7−10] Here the major challenges are centered around the stringent chemical and thermal sensitivity of organic semiconductors, whereby processing routes for the inorganic species that preserve the electro-optical properties of the organic species are required.[11−13] Several suggestions have been proposed for novel materials or processes, such that devices with organic layers interfaced with inorganic semiconductors exhibiting power conversion efficiencies (PCEs) over 10% have been reported.[14−16] The interlayer materials proposed share common features that are essential for successful device incorporation, namely, high optical transparency, selective charge transport, and tunable energy levels.

Processing temperature has emerged as perhaps the key property to control interlayer deposition; consequently, a number of low-temperature sol–gel chemistries have emerged alongside nanoparticle based synthesis and other wet chemical processing routes.[17−19] However, with many of these routes, issues of inhomogeneity persist and the challenges of complex chemistry prevent wide-scale uptake of these materials and methods. Recently it has been shown that a low-temperature (110 °C) solution based method for preparing ZnO electron transport layers (ETLs) can be successfully used in OPVs;[20]

Received: August 30, 2017
Revised: October 17, 2017
Published: October 30, 2017

DOI: 10.1021/acs.cgd.7b01222
Cryst. Growth Des. XXXX, XXX, XXX–XXX

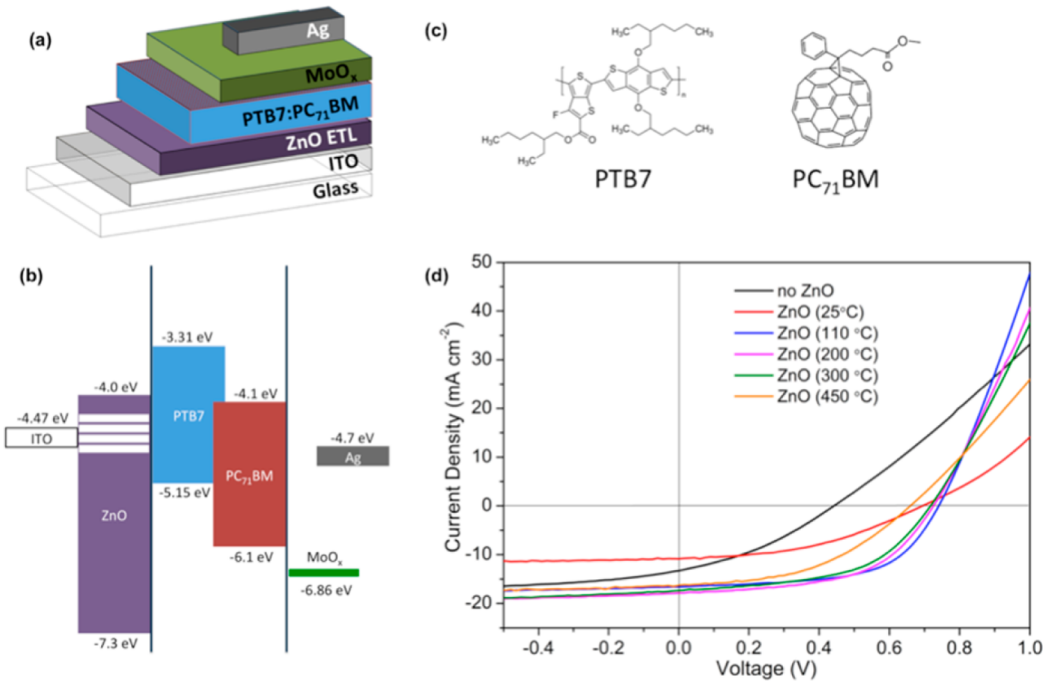

Figure 1. (a) Schematic illustration of inverted device architecture, (b) energy level diagram of devices, (c) molecular structure of electron donor (PTB7) and acceptor ($PC_{71}BM$) active layer materials, and (d) representative $J-V$ curves for devices prepared using ZnO electron transport layers (ETLs) deposited at the temperatures indicated.

here we utilize this material in high performance OPVs and elucidate their precise chemistry and composition in order to explain their excellent performance characteristics. Using PTB7:$PC_{71}BM$ active layers, we demonstrate devices incorporating our 110 °C processed ZnO with average PCEs exceeding 7% (champion device >8%). Using X-ray photoelectron spectroscopy (XPS) we study the change in the structure and bonding of the ETL as processing temperature is varied, and through the use of high resolution transmission electron microscopy (TEM) reveal the structure of the ETL to consist of ZnO nanoparticles embedded in an extended amorphous organic matrix. In addition to probing the local structure and chemistry of the ETLs, we employ transient photocurrent (TPC) and transient photovoltage (TPV) measurements to study the influence of ETL composition on device performance as a function of processing temperature.

2. MATERIALS AND METHODS

2.1. Solution Preparation. Indium tin oxide substrates (ITO, PsiOteC UK Ltd.; 12−16 Ω/sq) were cleaned using ultrasonics and sequential washing in acetone, isopropanol, and distilled water prior to being dried with compressed nitrogen gas followed by a 10 min UV-ozone clean (UVOCS).

ZnO sol−gel solutions were prepared by mixing equimolar quantities of zinc acetate dihydrate $Zn(CH_3COO)_2{\cdot}2H_2O$ and monoethanolamine ($HOCH_2CH_2NH_2$) in 2-methoxyethanol ($C_3H_8O_2$) followed by overnight stirring in ambient conditions.

Poly[[4,8-bis[(2-ethylhexyl)oxy]benzo[1,2-*b*:4,5-*b*′]dithiophene-2,6-diyl][3-fluoro-2-[(2-ethylhexyl)carbonyl]thieno[3,4-*b*]thiophene-4,6-diyl]] (PTB7) and [6,6]-phenyl-C71-butyric acid methyl ester ($PC_{71}BM$) (1:1.5 w/w) blends were dissolved in a mixed solvent of chlorobenzene and 1,8-diiodooctane (97:3 v/v) at a concentration of 25 mg/mL and heated at 60 °C with stirring overnight in a N_2 glovebox. Spin coating was carried out in a glovebox and the films were dried in a vacuum chamber for 20 min. Devices were completed evaporating 10 nm of MoO_3 followed by 100 nm of silver. The pixel area was 4.5 mm^2 as defined by the spatial overlap of the ITO and Ag electrodes.

2.2. ETL Characterization. Film thicknesses were measured using a surface profilometer (Dektak 150). ETLs studied by XPS were deposited directly onto the ITO substrates as described. The spectra were recorded on a Thermo Scientific K-Alpha$^+$ X-ray photoelectron spectrometer operating at 2×10^{-9} mbar base pressure. This system incorporates a monochromated, microfocused Al Kα X-ray source ($h\nu$ = 1486.6 eV) and a 180° double focusing hemispherical analyzer with a 2D detector. The X-ray source was operated at 6 mA emission current and 12 kV anode bias. Data were collected at 200 eV pass energy for survey, 20 eV pass energy for core level using an X-ray spot size of 400 μm^2. A flood gun was used to minimize sample charging. All data were analyzed using the Avantage software package.

TEM samples were prepared using a Helios NanoLab DualBeam to produce cross sections of complete devices. Ion beam accelerating voltages of 30, 5, and 2 kV were used sequentially. TEM and Scanning TEM (STEM) imaging was carried out using JEOL 2100F at 200 kV. Great care was taken to minimize the sample exposure to the electron beam.

Transient photovoltage and transient photocurrent measurements, white-light illumination was provided by a ring of 12 white LEDs capable of a power up to 7 suns, calibrated to device performance to 1 sun equivalent as measured under simulated AM1.5 illumination. An optical small perturbation is then applied to the device on top of the illumination background using a GL-330 PTI nitrogen laser pumped GL-301 PTI dye laser. Because TPV process was held in open-circuit condition, this small perturbation generated charge was forced to recombine. Through measuring the lifetime of extra carriers photogenerated by the laser pulse, the total lifetime of charge carrier within the device are able to be determined. The steady-state carrier density was determined by differential charging. Through measuring the small perturbation charge as used in TPV and voltage change, differential capacitance can be determined: $C = \Delta Q/\Delta V_0$. Then charge density can be integrated: $n = \frac{1}{Aed}\int_0^{V_0} c(V)\,dV$. TPC was measured at relatively low light intensity to minimize the influence of recombination. Voltage transients are measured on a Tektronix

DOI: 10.1021/acs.cgd.7b01222
Cryst. Growth Des. XXXX, XXX, XXX−XXX

TDS3032 oscilloscope and fitted with a monoexponential to obtain the small perturbation carrier lifetime.

Under open circuit condition upon different light intensity, the voltage applied matches with the quasi Fermi level splitting within the device, therefore the expected V_{OC} value as combination of energetic difference and recombination flux can be expressed as

$$V_{OC} = \frac{1}{e}(E_{VB} - E_{CB}) - \frac{n_{id}kT}{e}\ln\left(\frac{J_{rec}}{J_{SC}}\right)$$

where E_{VB} and E_{CB} are termed the effective band gaps and can be obtained from open circuit voltage dependent charge density. In the right side term, where n_{id} is the ideality factor, J_{rec} is the recombination current, and J_{SC} is short circuit current, which describes the recombination kinetics within the device.

2.3. Device Testing. OPV $J-V$ characteristics were measured using a xenon lamp (1 Sun, AM 1.5 G) (Oriel Instruments) with a Keithley 2400 source meter. Power conversion efficiency (PCE), open circuit voltage (V_{OC}), short circuit current density (J_{SC}), fill factor (FF), series resistance (R_s), and shunt resistance (R_{sh}) are calculated using the $J-V$ data. R_s and R_{sh} are extracted from the inverse slope of the $J-V$ curve at $I = 0$ and $V = 0$, respectively. Generally, a minimum of 10 devices were applied for each set of processing conditions.

3. RESULTS AND DISCUSSION

3.1. Device Fabrication and Performance Assessment. Devices were fabricated in the inverted architecture, with a typical structure (layer thicknesses in parentheses) of glass/ITO (140 nm)/ZnO (20 nm)/PTB7:$PC_{71}BM$ (110 nm)/MoO_x (10 nm)/Ag (100 nm), shown schematically in Figure 1a, alongside the relevant energy levels of the materials[20−22] in Figure 1b and molecular structure of the active layer materials Figure 1c. Both ZnO and the active layer were deposited from solution and the MoO_x/Ag thermally evaporated. Representative current−voltage ($J-V$) characteristics are shown in Figure 1d where the ZnO processing temperature is varied over the range 25−450 °C, also included is data for a device prepared without an ETL. Statistical data for all devices prepared are summarized in SI Figure 1. From these data it is clear that the ETL processing temperature is having a significant impact on device performance. Overall the best performing devices are observed at a processing temperature of 110 °C, where the champion device shows >8% PCE and average open-circuit voltage (V_{OC}), short-circuit current (J_{SC}), and fill-factor (FF) of 0.74 V, 16.3 mA/cm^2, and 65%, respectively. The device characteristics over the temperature range 110−300 °C are comparable, with a drop in performance observed at 450 °C, where the onset of crystallization in the ETL and a change in work function result in V_{OC} and FF losses.[20] The dark $J-V$ scans show improved blocking behavior at the lower processing temperatures (SI Figure 2); thus, our ETL fulfills the low-temperature and charge selective transport criteria desirable in such interlayers. Unsurprisingly poor performing devices are measured when no ETL is included in the device stack, and similar characteristics are observed when the ETL is processed at 25 °C, suggesting that a significant change in the ETL is occurring between 25 and 110 °C that enables efficient device operation.

A significant work function shift of the ETL with processing temperature plays the dominant role in device performance compared with other factors, i.e., surface morphology, optical transmission, and electrical properties.[20] When other organic active layer materials are employed the sensitivity to processing temperature over the 110−300 °C range is more profound than observed here with PTB7:$PC_{71}BM$, with significant V_{OC} and FF losses observed as temperature increases above 110 °C—attributed to pinning effects at the organic/ETL interface.[9,10] Specifically, if the work function of the ETL is lower than the electron affinity of the fullerene, the Fermi level (E_F) of the ETL becomes pinned to the LUMO level of the fullerene. As the LUMO of $PC_{71}BM$ is lower than that of ICBA (−3.91 eV vs −3.74 eV),[23] the E_F of the ETL is more likely to be pinned in the PTB7:$PC_{71}BM$ devices compared with the P3HT:ICBA devices.

While observing changes in device performance is indicative of changes occurring in the ETL, one may only speculate as to the origin of these variations. It is however critical to understand any changes in structure, bonding, and composition of these layers. To understand how ETL composition is changing with temperature we performed X-ray photoelectron spectroscopy (XPS) of ETL layers processed between 110 and 450 °C. Spectra of the C 1s and O 1s core levels are illustrated in Figure 2a and b, respectively, with data for the Zn 2p in SI Figure 3. From analysis of these data it is apparent that the carbon and oxygen signals are profoundly affected by processing temperature.

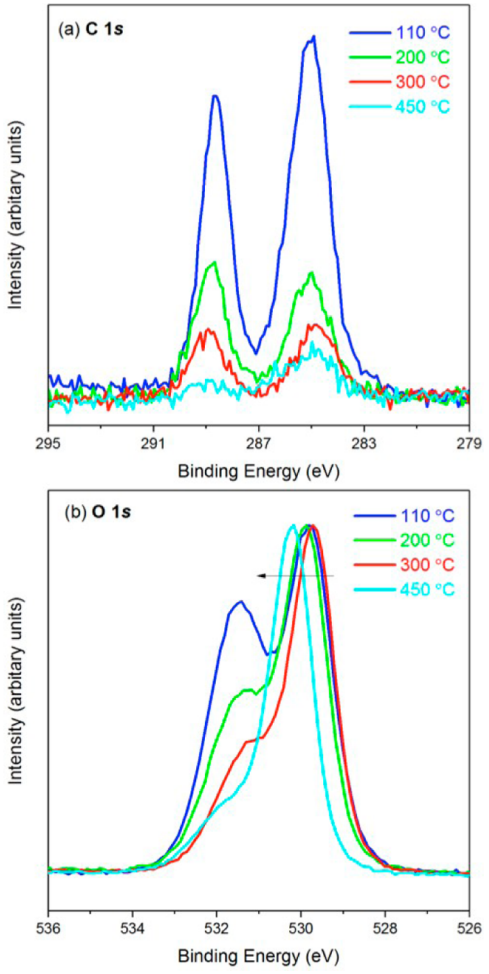

Figure 2. Obtained ZnO XPS spectra of (a) C 1s and (b) O 1s films processed at over the temperature range 110−450 °C.

3.2. Quantifying Morphological and Compositional Changes. At 110 °C the C 1s shows two distinct peaks at 288 and 285 eV, with the peak at higher binding energy characteristic of C═O, i.e., the carbonyl group of the acetate

DOI: 10.1021/acs.cgd.7b01222
Cryst. Growth Des. XXXX, XXX, XXX−XXX

precursor, and the lower energy signal originating from C−C bonds (including any surface carbon contamination). Both signals diminish as the temperature is increased with the C═O component almost vanishing at 450 °C. This data suggests that the ZnO precursor degrades and is thermally oxidized at a temperature somewhere between 300 and 450 °C, consistent with previous FTIR analysis.[20] The O 1s spectra show similar behavior where the sample heated at 110 °C displays a number of overlapping peaks, the lower binding energy peak assigned to Zn−O (oxide) peak and the higher binding energy assigned to the carbonyl group. There is also likely to be small contributions from −OH, trace precursor, and substoichiometry of the oxide,[24] but a detailed peak-fitting analysis of the O 1s core level is beyond the scope of this work. What can clearly be seen is a systematic decrease in the intensity of the carbonyl peak as the temperature increases relative to the Zn−O (oxide) peak. It is also observed that the position of the Zn−O (oxide) peak shifts from lower to higher binding energy upon annealing from 110 to 450 °C. This is indicative of a shift in the Fermi level position,[25] which we would expect to manifest itself as a rigid shift of the core levels, and is indeed what we see in the Zn−O (oxide) environment of the O 1s. Therefore, as a function of annealing we observe an increase in the work function of the material, a finding which is in excellent agreement with our previous Kelvin probe measurements on this system.[20]

To understand the structural evolution of the film we have used high-resolution transmission electron microscopy (HRTEM) (Figure 3). Previous characterization by X-ray diffraction (XRD) concluded that the ETLs prepared at 110 °C were amorphous; crystallinity was only detected when heated to 450 °C.[20] Here the TEM data clearly shows that the 110 °C processed ETL is composed of ZnO nanoparticles embedded in an amorphous matrix. Figure 3a shows the 110 °C annealed ETL between ITO and PTB7:$PC_{71}BM$ layers in a device structure where the nanocrystalline regions can be clearly seen; a number of measurable lattice spacings have been annotated corresponding to wurtzite ZnO. The inset shows a fast Fourier transform (FFT) confirming the presence of multiple crystalline domains in the film. From the combined XPS and TEM analysis we conclude that the ZnO nanocrystals are in a matrix composed of a complex mixture of precursor species, which is supported by the varying brightness seen within the ETL in scanning transmission electron microscopy (STEM) dark field imaging mode (Figure 3b). This observation is commensurate with our measurements of the 110 °C film optical bandgap[20] which at 3.38 eV is higher than anticipated owing to quantum confinement effects in ZnO nanoparticles.[26,27] This is further confirmed from the room temperature photoluminescence (PL) measurements that show a blueshift of near-band-edge emission compared to that of ZnO with higher temperatures, as shown in SI Figure 4.

The nanocrystalline/amorphous mixture also explains why the device with ZnO 110 °C works well, despite the low electron field effect mobility which is on the order of 10^{-5} times that of ZnO annealed at 300 °C.[20] In OPVs the free electrons only pass through ∼10 nm of the ETL as opposed to the long channel (several μm) in a TFT. In our OPVs the photogenerated electrons in the 110 °C processed ETL may be hopping between crystalline domains and tunneling in the organic matrix under the applied electric field. This charge transport process may be assisted by the conduction band minimum in ZnO which is dominated by Zn 2s orbitals; thus, the disorder of the ZnO crystalline structure has a rather weak influence on electron transport.[28] Rather than hindering the ETL performance, the amorphous region, rich in the sol−gel stabilizer monoethanolamine (MEA),[29] is acting as a work function modifier,[20,30,31] which has been demonstrated previously using ZnO nanoparticles and MEA as a dispersal solvent.[32] There may also be an advantage to preserving the organic matrix in that the densification observed in crystalline films, which may create pinholes, does not occur thus

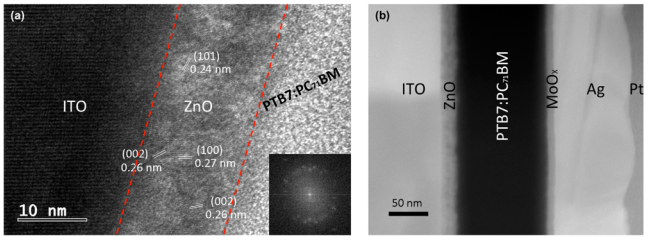

Figure 3. (a) HRTEM image showing the 110 °C annealed ZnO layer between the ITO and PTB7:$PC_{71}BM$ layers within the device. (b) STEM dark field image of full device showing, from left to right, the ITO, 110 °C ZnO, PTB7:$PC_{71}BM$, MoO_x, and Ag layers.

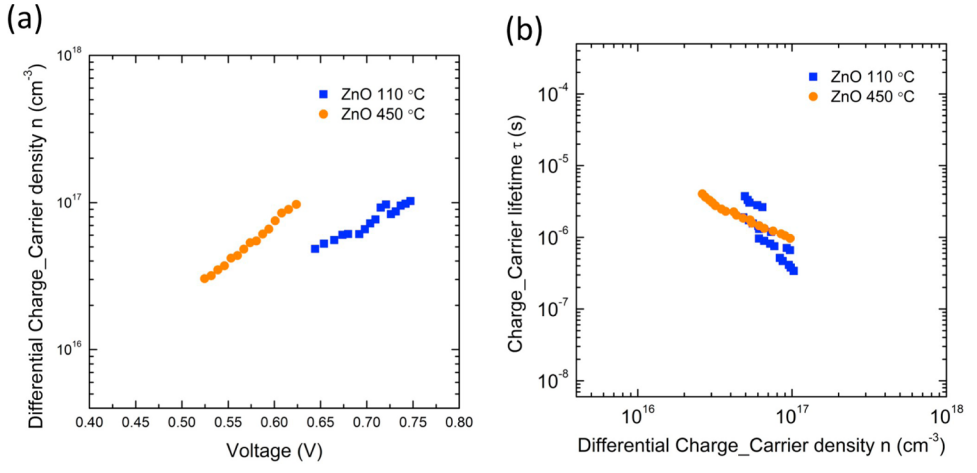

Figure 4. Device charge carrier density and lifetime measurements of PTB7:$PC_{71}BM$ solar cells with ZnO ETL processed at 110 and 450 °C: (a) Transient photocurrent (TPC) and (b) Transient photovoltage (TPV).

DOI: 10.1021/acs.cgd.7b01222
Cryst. Growth Des. XXXX, XXX, XXX−XXX

explaining the low leakage currents observed. Similarly, the organic matrix may also suppress the defect-induced subgap states in ZnO, a mechanism by which performance enhancements have been achieved in OPVs.[33,34] In comparison to complex nanoparticle synthesis, our current work illustrates a rather simple means of fabricating ZnO nanoparticle/amorphous organic matrices and opens the possibility of controlled mixing and doping for compositional variation and further control of the electro-optical properties.

3.3. Transient Optoelectronic Probes. To investigate the influence of ETL processing temperature on device performance, and particularly the V_{OC} increases observed at lower processing temperatures, charge carrier densities and lifetime were measured using transient photocurrent (TPC) and transient photovoltage (TPV) measurements for devices employing the 100 and 450 °C processed ETL layers. The charge density (n) at V_{OC} measured through differential charging is plotted in Figure 4a, while Figure 4b shows the charge carrier lifetimes (τ) measured as a function of n. These data give a good reconstruction of light intensity for both devices, confirming the validity of these data, as shown in SI Figure 5. The major difference between 110 and 450 °C is the large shift in V_{OC} at a given n, corresponding to 160 mV at $n = 5 \times 10^{16}$ cm^{-3}, while at the same density the charge carrier lifetimes are very similar for both temperatures. These data are analogous to those observed for PCDTBT:PCBM devices as a function of NiO hole collection layer work function, and assigned by correlation with numerical device modeling to the effect of surface recombination losses.[35] Specifically n is a measure of quasi-Fermi level splitting in the photoactive layer of the device. As such, following ref 35, the observation of a lower V_{OC} for the 450 °C processed device at same n indicates an interfacial voltage loss resulting from increased surface recombination losses; here, holes are collected by the ZnO side reducing quasi-Fermi level splitting. Such increased surface recombination losses are consistent due to the higher ZnO work function caused by high temperature processing. We note that due to the high shunt dark current in 450 °C device (SI Figure 5), it was not possible to analyze device factors in terms of surface recombination losses. These data therefore confirm that the higher V_{OC} of device with ZnO 110 °C mainly comes from a lower ZnO work function reducing surface recombination losses.

4. CONCLUSIONS

Here we demonstrate the incorporation of a low-temperature processed electron transport layer comprising nanocrystalline ZnO embedded in an organic amorphous matrix in high performing organic photovoltaic devices. Using a combination of X-ray photoelectron spectroscopy and transmission electron microscopy we follow the structural and compositional evolution of the ETL as a function of processing temperature. Our ETLs are processed using a remarkably simple solution processing route, and using transient optoelectronic probes, we demonstrate that the mixed nanocrystalline/amorphous nature of the films does not contribute to recombination losses in devices. Indeed the presence of the stabilizer used for preparation of the sol–gel precursor, which remains present in the low-temperature processed films, acts as an efficient work function modifier. Our objective was to develop a low-temperature, solution-processable charge selective interlayer for organic photovoltaic devices that had high optical transparency and good charge transport. The ETL we have developed fulfills the criteria for OPV interlayers and for the future development of devices that are compatible with high throughput processing.

■ ASSOCIATED CONTENT

Supporting Information

The Supporting Information is available free of charge on the ACS Publications website at DOI: 10.1021/acs.cgd.7b01222.

Statistical data of OPVs, dark $J-V$ curves of OPVs, Zn 2p XPS spectra of ZnO, PL spectra of ZnO, V_{OC} reconstruction from TPC and TPV (PDF)

■ AUTHOR INFORMATION

Corresponding Author

*E-mail: martyn.mclachlan@imperial.ac.uk.

ORCID

Maurizio Morbidoni: 0000-0003-3943-3551
James R. Durrant: 0000-0001-8353-7345
Martyn A. McLachlan: 0000-0003-3136-1661

Notes

The authors declare no competing financial interest.

■ ACKNOWLEDGMENTS

J.Z. and M.A.M. thank the China Scholarship Council for financial support for PhD studies. K.H. and M.A.M. the National Plan for Science, Technology and Innovation (MAARIFAH) - King Abdulaziz City for Science and Technology - for funding through the Science & Technology Unit at KFUPM award (12-ENE2379-04). D.J.P. acknowledges support from the Royal Society (UF150693) and the EPSRC (EP/M028291/1). M.A.M. and J.R.D. are grateful for continued support through the EPSRC Centre for Doctoral Training in Plastic Electronics (EP/L016702/1).

■ REFERENCES

(1) Zou, J.; Li, C. Z.; Chang, C. Y.; Yip, H. L.; Jen, A. K. Y. Interfacial Engineering of Ultrathin Metal Film Transparent Electrode for Flexible Organic Photovoltaic Cells. *Adv. Mater.* **2014**, *26*, 3618–3623.

(2) Krebs, F. C.; Espinosa, N.; Hosel, M.; Sondergaard, R. R.; Jorgensen, M. 25th Anniversary Article: Rise to Power - OPV-Based Solar Parks. *Adv. Mater.* **2014**, *26* (1), 29–39.

(3) Brabec, C. J.; Dyakonov, V.; Parisi, J.; Sariciftci, N. S. *Organic Photovoltaics*; Springer, 2003.

(4) Yau, C. P.; Wang, S.; Treat, N. D.; Fei, Z.; Tremolet de Villers, B. J.; Chabinyc, M. L.; Heeney, M. Investigation of Radical and Cationic Cross-Linking in High-Efficiency, Low Band Gap Solar Cell Polymers. *Adv. Energy Mater.* **2015**, *5*, 1401228.

(5) Fei, Z.; Kim, J. S.; Smith, J.; Domingo, E. B.; Anthopoulos, T. D.; Stingelin, N.; Watkins, S. E.; Kim, J.-S.; Heeney, M. A Low Band Gap Co-Polymer of Dithienogermole and 2,1,3- Benzothiadiazole by Suzuki Polycondensation and Its Application in Transistor and Photovoltaic Cells. *J. Mater. Chem.* **2011**, *21*, 16257.

(6) Sekine, C.; Tsubata, Y.; Yamada, T.; Kitano, M.; Doi, S. Recent Progress of High Performance Polymer OLED and OPV Materials for Organic Printed Electronics. *Sci. Technol. Adv. Mater.* **2014**, *15*, 34203.

(7) Hewlett, R. M.; McLachlan, M. A. Surface Structure Modification of ZnO and the Impact on Electronic Properties. *Adv. Mater.* **2016**, *28*, 3893–3921.

(8) Meyer, J.; Hamwi, S.; Kröger, M.; Kowalsky, W.; Riedl, T.; Kahn, A. Transition Metal Oxides for Organic Electronics: Energetics, Device Physics and Applications. *Adv. Mater.* **2012**, *24*, 5408–5427.

(9) Greiner, M. T.; Lu, Z. H. Thin-Film Metal Oxides in Organic Semiconductor Devices: Their Electronic Structures, Work Functions and Interfaces. *NPG Asia Mater.* **2013**, *5*, e55.

DOI: 10.1021/acs.cgd.7b01222
Cryst. Growth Des. XXXX, XXX, XXX–XXX

(10) Greiner, M. T.; Helander, M. G.; Tang, W.-M.; Wang, Z.-B.; Qiu, J.; Lu, Z.-H. Universal Energy-Level Alignment of Molecules on Metal Oxides. *Nat. Mater.* **2011**, *11*, 76−81.
(11) Zilberberg, K.; Meyer, J.; Riedl, T. Solution Processed Metal-Oxides for Organic Electronic Devices. *J. Mater. Chem. C* **2013**, *1*, 4796−4815.
(12) Franklin, J. B.; Downing, J. M.; Giuliani, F.; Ryan, M. P.; McLachlan, M. A. Building on Soft Foundations: New Possibilities for Controlling Hybrid Photovoltaic Architectures. *Adv. Energy Mater.* **2012**, *2*, 528−531.
(13) Franklin, J. B.; Gilchrist, J. B.; Downing, J. M.; Roy, K. A.; McLachlan, M. A. Transparent Conducting Oxide Top Contacts for Organic Electronics. *J. Mater. Chem. C* **2014**, *2*, 84−89.
(14) Green, M. A.; Emery, K.; Hishikawa, Y.; Warta, W.; Dunlop, E. D. Solar Cell Efficiency Tables (Version 48). *Prog. Photovoltaics* **2016**, *24*, 905−913.
(15) Zhang, S.; Ye, L.; Hou, J. Breaking the 10% Efficiency Barrier in Organic Photovoltaics: Morphology and Device Optimization of Well-Known PBDTTT Polymers. *Adv. Energy Mater.* **2016**, *6*, 1502529.
(16) Jagadamma, L. K.; Al-Senani, M.; El-Labban, A.; Gereige, I.; Ngongang Ndjawa, G. O.; Faria, J. C. D.; Kim, T.; Zhao, K.; Cruciani, F.; Anjum, D. H.; McLachlan, M. A.; Beaujuge, P. M.; Amassian, A. Polymer Solar Cells with Effi Ciency > 10% Enabled via a Facile Solution-Processed Al- Doped ZnO Electron Transporting Layer. *Adv. Energy Mater.* **2015**, *5*, 1500204.
(17) Lee, Y.-J.; Yi, J.; Gao, G. F.; Koerner, H.; Park, K.; Wang, J.; Luo, K.; Vaia, R. A.; Hsu, J. W. P. Low-Temperature Solution-Processed Molybdenum Oxide Nanoparticle Hole Transport Layers for Organic Photovoltaic Devices. *Adv. Energy Mater.* **2012**, *2*, 1193−1197.
(18) Lin, Y. H.; Faber, H.; Zhao, K.; Wang, Q.; Amassian, A.; McLachlan, M. A.; Anthopoulos, T. D. High-Performance ZnO Transistors Processed Via an Aqueous Carbon-Free Metal Oxide Precursor Route at Temperatures Between 80−180 °C. *Adv. Mater.* **2013**, *25*, 4340−4346.
(19) Krishnan Jagadamma, L.; Abdelsamie, M.; El Labban, A.; Aresu, E.; Ngongang Ndjawa, G. O.; Anjum, D. H.; Cha, D.; Beaujuge, P.; Amassian, A. Efficient Inverted Bulk- Heterojunction Solar Cells from Low-Temperature Processing of Amorphous ZnO Buffer Layers. *J. Mater. Chem. A* **2014**, *2*, 13321−13331.
(20) Zhang, J.; Faria, J. C. D.; Morbidoni, M.; Porte, Y.; Burgess, C. H.; Harrabi, K.; McLachlan, M. A. Low-Temperature Solution-Processed Electron Transport Layers for Inverted Polymer Solar Cells. *Adv. Electron. Mater.* **2016**, *2*, 1600008.
(21) Ouyang, X.; Peng, R.; Ai, L.; Zhang, X.; Ge, Z. Efficient Polymer Solar Cells Employing a Non-Conjugated Small-Molecule Electrolyte. *Nat. Photonics* **2015**, *9*, 520−524.
(22) Kröger, M.; Hamwi, S.; Meyer, J.; Riedl, T.; Kowalsky, W.; Kahn, A. P-Type Doping of Organic Wide Band Gap Materials by Transition Metal Oxides: A Case-Study on Molybdenum Trioxide. *Org. Electron.* **2009**, *10*, 932−938.
(23) Cheng, P.; Li, Y.; Zhan, X. Efficient Ternary Blend Polymer Solar Cells with Indene-C60 Bisadduct as an Electron-Cascade Acceptor. *Energy Environ. Sci.* **2014**, *7*, 2005.
(24) MacLeod, B. A.; Tremolet de Villers, B. J.; Schulz, P.; Ndione, P. F.; Kim, H.; Giordano, A. J.; Zhu, K.; Marder, S. R.; Graham, S.; Berry, J. J. Stability of Inverted Organic Solar Cells with ZnO Contact Layers Deposited from Precursor Solutions. *Energy Environ. Sci.* **2015**, *8*, 592−601.
(25) Seal, K.; Jesse, S.; Nikiforov, M. P.; Kalinin, S. V.; Fujii, I.; Bintachitt, P.; Trolier-McKinstry, S. Spatially Resolved Spectroscopic Mapping of Polarization Reversal in Polycrystalline Ferroelectric Films: Crossing the Resolution Barrier. *Phys. Rev. Lett.* **2009**, *103*, 057601.
(26) Lu, J. G.; Ye, Z. Z.; Zhang, Y. Z.; Liang, Q. L.; Fujita, S.; Wang, Z. L. Self-Assembled ZnO Quantum Dots with Tunable Optical Properties. *Appl. Phys. Lett.* **2006**, *89*, 023122.
(27) Cheng, H. M.; Lin, K. F.; Hsu, H. C.; Hsieh, W. F. Size Dependence of Photoluminescence and Resonant Raman Scattering from ZnO Quantum Dots. *Appl. Phys. Lett.* **2006**, *88*, 261909.
(28) Ginley, D. S.; Perkins, J. D. *Handbook of Transparent Conductors*; 2011.
(29) Ohyama, M.; Kouzuka, H.; Yoko, T. Sol-Gel Preparation of ZnO Films with Extremely Preferred Orientation along (002) Plane from Zinc Acetate Solution. *Thin Solid Films* **1997**, *306*, 78−85.
(30) Zhou, Y.; Fuentes-hernandez, C.; Shim, J.; Meyer, J.; Giordano, A. J.; Li, H.; Winget, P.; Papadopoulos, T.; Cheun, H.; Kim, J. A Universal Method to Produce Low−Work Function Electrodes for Organic Electronics. *Science* **2012**, *336*, 327−332.
(31) Lee, Y. J.; Wang, J.; Cheng, S. R.; Hsu, J. W. P. Solution Processed ZnO Hybrid Nanocomposite with Tailored Work Function for Improved Electron Transport Layer in Organic Photovoltaic Devices. *ACS Appl. Mater. Interfaces* **2013**, *5*, 9128−9133.
(32) Jeon, I.; Ryan, J. W.; Nakazaki, T.; Yeo, K. S.; Negishi, Y.; Matsuo, Y. Air-Processed Inverted Organic Solar Cells Utilizing a 2-Aminoethanol-Stabilized ZnO Nanoparticle Electron Transport Layer That Requires No Thermal Annealing. *J. Mater. Chem. A* **2014**, *2*, 18754−18760.
(33) Wu, B.; Wu, Z.; Yang, Q.; Zhu, F.; Ng, T.; Lee, C.; Cheung, S.; So, S. Improvement of Charge Collection and Performance Reproducibility in Inverted Organic Solar Cells by Suppression of ZnO Subgap States. *ACS Appl. Mater. Interfaces* **2016**, *8*, 14717−14724.
(34) Wu, Z.; Wu, B.; Tam, H. L.; Zhu, F. An Insight on Oxide Interlayer in Organic Solar Cells: From Light Absorption and Charge Collection Perspectives. *Org. Electron.* **2016**, *31*, 266−272.
(35) Wheeler, S.; Deledalle, F.; Tokmoldin, N.; Kirchartz, T.; Nelson, J.; Durrant, J. R. Influence of Surface Recombination on Charge-Carrier Kinetics in Organic Bulk Heterojunction Solar Cells with Nickel Oxide Interlayers. *Phys. Rev. Appl.* **2015**, *4*, 29−31.

DOI: 10.1021/acs.cgd.7b01222
Cryst. Growth Des. XXXX, XXX, XXX−XXX